

# How Transition Metals Enable Electron Transfer through the SEI: Part I. Experiments and Butler-Volmer Modeling

Oliver C. Harris, 61,\* Yuxiao Lin, Yue Qi,2,\*\* Kevin Leung,3,\*\* and Maureen H. Tang 61,\*\*,z

Transition metal dissolution from high-voltage Li-ion battery cathodes disrupts the formation and performance of the solid-electrolyte interphase (SEI). SEI contamination by transition metals results in continual Li loss and severe capacity fade. Fundamental understanding of how metals undermine SEI passivation is necessary to mitigate this degradation. This two-part study interrogates the mechanisms by which transition metals facilitate through-film charge-transfer and SEI failure. Part I presents experimental results in which we intentionally contaminate SEIs with Mn, Ni, and Co. Rotating disk electrode voltammetry of a redox mediator quantifies how each metal impacts the charge-transfer characteristics of the SEI. A physics-based model finds that all three metals disrupt the electronic properties of the SEI more than the morphology. Surprisingly, the Butler-Volmer kinetics of charge-transfer through a Mn-contaminated SEI are an order of magnitude faster than for a Co-contaminated SEI, even with similar embedded metal concentrations. Such trends between metals are inconsistent with bandgap predictions from density functional theory, implying an alternative redox-cycling mechanism, which is mathematically developed and compared to experiment in Part II.

© The Author(s) 2019. Published by ECS. This is an open access article distributed under the terms of the Creative Commons Attribution 4.0 License (CC BY, http://creativecommons.org/licenses/by/4.0/), which permits unrestricted reuse of the work in any medium, provided the original work is properly cited. [DOI: 10.1149/2.0022001JES]

Manuscript submitted May 28, 2019; revised manuscript received July 24, 2019. Published August 26, 2019. This paper is part of the JES Focus Issue on Mathematical Modeling of Electrochemical Systems at Multiple Scales in Honor of Richard Alkire.

High-voltage Li-ion batteries (LIBs) are an important technology to unlock widespread electric vehicle adoption, though current battery packs are heavy and only allow a limited driving range per charge. To progress vehicle electrification, energy dense battery materials are needed to increase driving range without sacrificing the weight of the battery pack. A promising target for increasing energy density is the cathode material. Many transition metal oxide cathodes operate at higher voltages, which increases battery capacity without adding weight. However, commercialization of these cathodes requires understanding and preventing a major issue: metal dissolution and associated capacity fade.

During high-voltage LIB operation (i.e. above 4.5 V vs. Li/Li<sup>+</sup>), electrolyte oxidation and metal dissolution occur. 1-10 While the loss of active material from the cathode undeniably diminishes electrode capacity, the primary mechanism of full-cell capacity fade is loss of cyclable lithium at the anode. Loss of cyclable lithium is accelerated by electrode crosstalk, where dissolved species from the positive electrode interfere with important protective processes at the negative electrode.<sup>2,7,11,12</sup> This is evident when comparing the effect of lost cathode active material to the effect of metal deposition at the negative electrode. Choi reported total metal dissolution rates of less than 2% for layered NMC (LiNi $_x$ Mn $_y$ Co $_z$ ) electrodes, compared to 0.8% cobalt dissolution from LiCoO<sub>2</sub><sup>11</sup>. Pieczonka demonstrated good capacity retention for LNMO/Li and graphite/Li half-cells, whereas LNMO/graphite full-cells exhibited poor retention, indicating that active material loss alone does not dominate capacity fade. 13 However, even at low concentrations, metal accumulation at the negative electrode has severe consequences for battery lifetime. For instance, Gilbert et al. found over 50% capacity loss in NMC532/graphite fullcells with metal deposition less than 0.5% weight fraction.<sup>3</sup> Many other groups have documented the deleterious effects of transition metal deposition at the negative electrode<sup>2–4,7,12–28</sup> further confirming that deposition is a more important capacity loss mechanism than active material loss from the cathode.

Metal deposition at the negative electrode accelerates capacity fade by disrupting the formation and growth of the solid-electrolyte interphase (SEI), arguably the most important interface in LIBs. The SEI is a passivating film formed on the negative electrode when the electrolyte decomposes at low voltages and this film is chiefly responsible for protecting the electrolyte from continual reduction by the negative electrode during long-term cycling. <sup>29–31</sup> We previously showed that the SEI protects the electrolyte primarily because inorganic components block electron transport through the film, whereas organic SEI components have little or no contribution to the protective nature. <sup>32</sup> When metals contaminate the SEI, the ability to block through-film electron transport is hindered. Thus, failure of SEI passivation by metal deposition results in constant Li consumption, electrolyte breakdown, and accelerated capacity fade.

As this issue has been investigated since Tarascon found that Mn dissolution from LMO (LiMn<sub>2</sub>O<sub>4</sub>) spinel accelerated battery failure,  $^{33}$  the effects of metal contamination have mostly been qualified via spectroscopy and quantified by tracking coulombic efficiency and discharge capacity degradation over cycling. Postmortem analyses and in situ studies have determined metal oxidation states  $^{3,4,7,10,12,13,15,16,19-23,26,34-37}$  and quantities within the SEI,  $^{4,5,11,27}$  yet these approaches have not yet explained how these metals facilitate through-film charge transfer.

This work seeks to specifically address the mechanism by which metals corrupt the SEI and to explain why Mn is uniquely pernicious. We interrogate the individual effects of the transition metals (Mn, Ni, and Co) in NMC electrodes on charge-transfer through the SEI via in-situ electrochemical characterization. Similar to our previous work, 32,38,39,39-41 we grow an SEI in metal-contaminated electrolyte and then characterize the film via rotating disk electrode voltammetry using ferrocenium as a redox probe of the SEI. The advantage of studying through-film ferrocenium reduction, compared to full-cell coulombic efficiency tracking, is that our approach can deconvolute electronic from ionic charge transfer, providing interface-scale understanding of metal-induced capacity fade. Part I of this work presents the experimental data and interprets measurements with a previously developed model based on charge-transfer at pinholes in the SEI.<sup>32</sup> We find that all three metals present in NMC electrodes disrupt the electronic properties of the SEI more than the morphological properties, and that Mn is the most disruptive of the three. We employ a physics-based model to rationalize why Mn is exceptional and find that previous models based on Butler-Volmer kinetics are insufficient to describe the trends between metals. Additionally, these trends disagree with predictions from Density Functional Theory (DFT), suggesting an alternative mechanism of SEI corruption by metals.

<sup>&</sup>lt;sup>1</sup>Drexel University, Philadelphia, Pennsylvania 19104, USA

<sup>&</sup>lt;sup>2</sup>Department of Chemical Engineering and Materials Science, Michigan State University East Lansing, Michigan 48824, USA

<sup>&</sup>lt;sup>3</sup>Sandia National Laboratory, Albuquerque, New Mexico 87185, USA

<sup>\*</sup>Electrochemical Society Student Member.

<sup>\*\*</sup>Electrochemical Society Member.

<sup>&</sup>lt;sup>z</sup>E-mail: mhtang@drexel.edu

In Part II of this work<sup>55</sup> we develop a microkinetic model of a different mechanism based on electrocatalytic metal cycling<sup>4,22,23,25,42</sup> within the SEI and interpret experimental results from Part I through this model to explain enhanced through-SEI charge-transfer.

#### **Experimental and Computational Methods**

**Preparation of electrodes and electrolytes.**—Prior to use, 5 mm outer-diameter glassy carbon disk electrodes (Pine Research) were gently polished with  $1.0~\mu m$  alumina MicroPolish (Buehler) on a nylon polishing cloth (BASi), sonicated in deionized water for 15 min to remove alumina particles, and then dried under vacuum. Dried electrodes were inserted into PTFE shrouds (Pine Research), transferred to an Ar-filled glove box (LC Technology Solutions) and mounted on a rotating ring disk (RDE) assembly (Pine Research).

The base electrolyte was commercial 1 M LiPF<sub>6</sub> in ethylene carbonate (EC) and dimethyl carbonate (DMC) (1:1, v:v) (LP 30 Gotion). Manganese (III) acetylacetonate (Mn(AcAc)<sub>3</sub>, technical grade, Sigma Aldrich), nickel (II) acetylacetonate (Ni(AcAc)<sub>2</sub>, 95%, Sigma Aldrich), and cobalt (III) acetylacetonate (Co(AcAc)<sub>3</sub>, 98%, Sigma Aldrich) were added to the electrolyte to yield a metal concentration of 25 mM. For testing, 1 mL of these concentrated solutions were added to 11.5 mL of metal-free electrolyte to reach a final concentration of 2 mM.

**Electrochemical measurements.**—Measurements were performed in custom-made glass cells containing  $\sim 12$  mL of electrolyte, Li reference electrodes, and either Li or Pt counter electrodes. Reference and counter electrodes were isolated from the bulk electrolyte by fritted gas dispersion tubes which limited electrode oxidation by the transition metal ions. When a frit was not used, the open-circuit voltage of the Li drifted significantly and the electrode color became black.

For each experimental trial, the glassy carbon disc working electrode was cycled between 3 and 0.1 V vs. Li/Li+ at 20 mV/s for three cycles to grow a solid-electrolyte interphase (SEI) passivating film. After formation, the working electrode was transferred to a second custom-made glass cell containing ~12 mL of approximately 2 mM each ferrocene and ferrocenium hexafluorophosphate (Sigma Aldrich) in metal-free LP 30 electrolyte. Cyclic voltammograms of ferrocenium reduction through the passivating films were collected between 2 and 3.3 V vs. Li/Li<sup>+</sup> at 20 mV/s and 400, 900, and 1600 RPM rotation rates. To fit the experimental data to a theoretical model, the anodic and cathodic currents of the voltammogram were averaged for each measured voltage in the sweep. A single glassy carbon disc was assigned to each of the three transition metals investigated (Mn, Ni, and Co) to avoid metal cross-contamination. The experimental procedure of SEI formation and ferrocenium reduction was performed at least three times on each glassy carbon disk for the case of a metal-doped electrolyte and the case of a metal-free electrolyte, totaling at least six tests for each disc. After use, the glassy carbon disc electrodes were cleaned via electrochemical oxidation of surface films, <sup>38–40</sup> and then polished as above.

*Computational details.*—For transition metal (M) doped structures, Density Functional Theory (DFT) implemented in VASP code  $^{43-45}$  was used for the spin polarizated electronic structure calculations, with the Perdew-Burke-Ernzerhof (PBE) functional,  $^{46}$  and the rotationally invariation DFT+U augmentation  $^{47}$  with (U-J) = 4.84, 5.95, and 3.30eV for Mn, Ni, and Co, respectively. For LiF, a 400 eV energy cutoff and 2  $\times$  2  $\times$  2 Brillouin zone sampling were used. In a simulation box containing 108 LiF, one Li+ was substituted by one M, to mimic M+. To generate a M²+, another Li+ about 3 Å away was also removed to yield asimulation cell containing 106 Li, 108 F, and 1  $M^{2+}$  ion.

For the M doping in  $\text{Li}_2\text{CO}_3$ , a 800 eV cutoff energy,  $4 \times 4 \times 4$  K-points Brillouin zone sampling, and DFT+U Hubbard U parameter of 3.9, 6.2, and 3.3 eV for Mn, Ni, and Co, respectively, were used. In

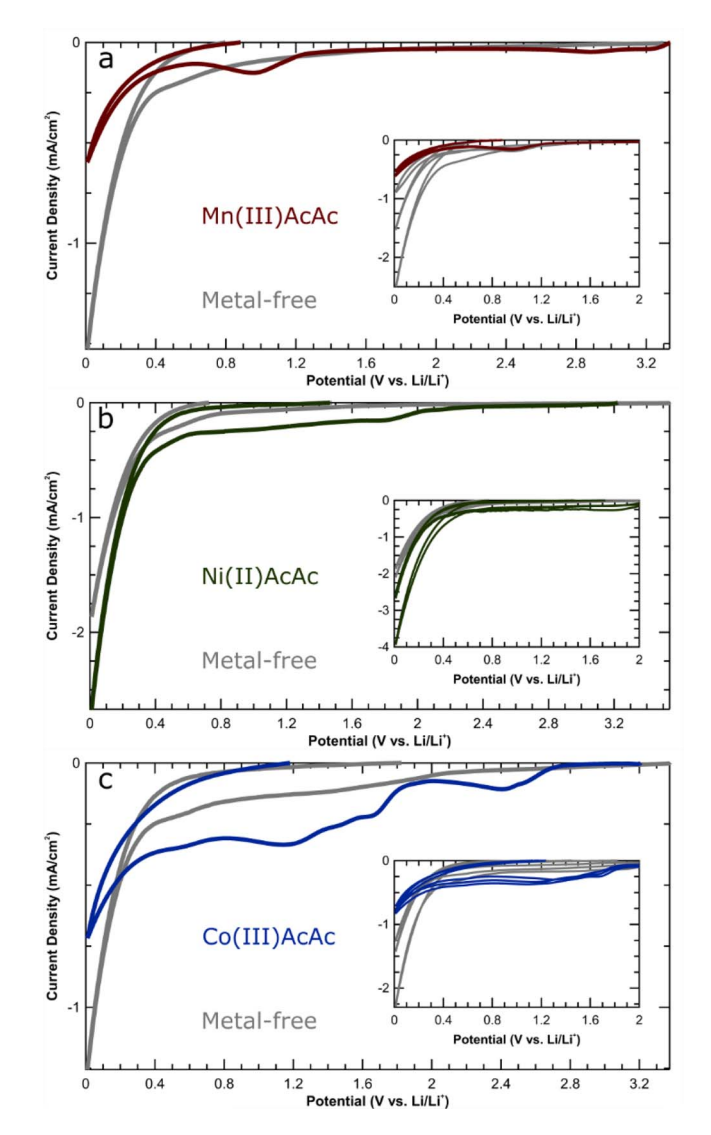


Figure 1. Transition metals alter SEI formation profiles. (a) SEI formation cyclic voltammograms on glassy carbon disc electrode in Mn-containing and Mn-free electrolytes. (b) SEI formation cyclic voltammograms on glassy carbon disc electrode in Ni-containing and Ni-free electrolytes. (c) SEI formation cyclic voltammograms on glassy carbon disc electrode in Co-containing and Co-free electrolytes. First cycle of three cycles shown, insets show SEI formation voltammograms for the three metal-contaminated trials and three metal-free trials on the same glassy carbon electrode.

a conventional cell containing four  $Li_2CO_3$ , one  $Li^+$  was substituted by one M and the nearest  $Li^+$  from M was also removed, resulting in a cell mimicing  $M^{2+}$  doping due to charge neutrality. In another test, two excess electrons were added to the simulation cell to mimic reduced M in the  $Li_2CO_3$  lattice. The high dopant concentration in  $Li_6MC_4O_{12}$  amplified the effect of the transition metal doping.

## **Results and Discussion**

Effect of transition metals on SEI formation.—We have previously studied SEI formation in organic carbonate electrolytes in the absence of transition metals<sup>38–41,48</sup> and developed methods to characterize the passivity of the formed SEI.<sup>32,38–41,48</sup> Applying the same methodologies here determines how transition metals impact the electrolyte reduction and decomposition reactions responsible for SEI formation and growth. Figure 1 shows SEI formation cyclic voltammograms, in which the glassy carbon disc electrode potential is swept between 0.01 V and 3 V vs. Li/Li<sup>+</sup> at 20 mV/s for three total

cycles. Grey lines indicate trials on the same glassy carbon disc with a metal-free electrolyte, while colored lines represent trials with transition metal salts in the electrolyte (1a, Mn(AcAc)<sub>3</sub>; 1b, Ni(AcAc)<sub>2</sub>; and 1c, Co(AcAc)<sub>3</sub>). For clarity, only the first cycle is shown.

Figure 1 demonstrates that each transition metal uniquely disrupts the electrolyte reduction reactions at low potentials that form and grow the SEI. In Figure 1a, the presence of Mn introduces new reduction peaks near 3.2, 2.8, and 0.95 V vs. Li/Li+ that are not present in metal-free electrolytes. The higher potential peaks are most likely reduction of Mn from the Mn<sup>3+</sup> oxidation state to Mn<sup>2+</sup> state, while the  $0.95\ V$  reduction peak is consistent with  $Mn^{2+}$  reduction as observed by Solchenbach and Jung et al. 24,37 The inset of Figure 1a shows that SEI formation with Mn present is very repeatable, while formation in metal-free electrolyte shows more variation from test to test. Also consistent with Solchenbach's and Jung's work, Figure 1b shows reduction peaks near 2.4 and 1.8 V vs. Li/Li+ which can be attributed to Ni<sup>2+</sup> reduction. In Figure 1c, Co appears to cause new reduction peaks near 2.4, 1.65, and 1.1 V vs. Li/Li+. We attribute the high potential reduction peak to Co<sup>3+</sup> reduction to Co<sup>2+</sup>, and expect that the lower potential reduction peaks correspond to Co<sup>2+</sup> reduction. Overall, each of these transition metals clearly interferes with the electrolyte reduction processes necessary to form the passivating SEI film.

Although the transition metals were introduced to the electrolyte as  $Mn^{3+}$ ,  $Ni^{2+}$ , and  $Co^{3+}$ , the voltammograms in Figure 1 show reduction

peaks for Mn and Co that suggest reduction to the 2+ valence state. Peaks are also present for Mn, Ni, and Co that suggest reduction of the 2+ metals, consistent with findings by Jung and Solchenbach using M(TFSI)<sub>2</sub> salts.<sup>24,37</sup> Mn(III) acetylacetonate was chosen for this work because Jarry, using X-ray fluorescence (XRF) and X-ray absorption near-edge structure (XANES), found Mn(III) acetylacetonate on cycled LiNi<sub>0.5</sub>Mn<sub>1.5</sub>O<sub>4</sub>, indicating Mn dissolves into the electrolyte in the +3 valence state. 26 In the same study, Jarry found that Mn on cycled graphite was mostly Mn(II) acetylacetonate with the remainder Mn(II) oxalate. 26 Additionally, we performed control experiments comparing the effect of electrolyte contamination by Mn(II) acetylacetonate to Mn(III) acetylacetonate, and found no significant difference in SEI performance. Thus, introducing Mn to the electrolyte in the +3 valence state is most similar to how Mn dissolves into the electrolyte from a positive electrode in a battery, and we rationalize that all three metals within the SEI are reduced from the +2 valence state. Accordingly, the remainder of this work does not explicitly specify the valence state of Mn, Ni, and Co in the SEI.

Scanning electron microscopy (SEM) and energy dispersive X-ray (EDX) were performed on metal-contaminated SEI samples to estimate the concentration of the metals within the films. Figures 2a, 2b, and 2c show the EDX spectra for an SEI contaminated by Mn, Ni, and Co, respectively, and demonstrate that the signals for these metals are weak compared to the other elements in the elec-

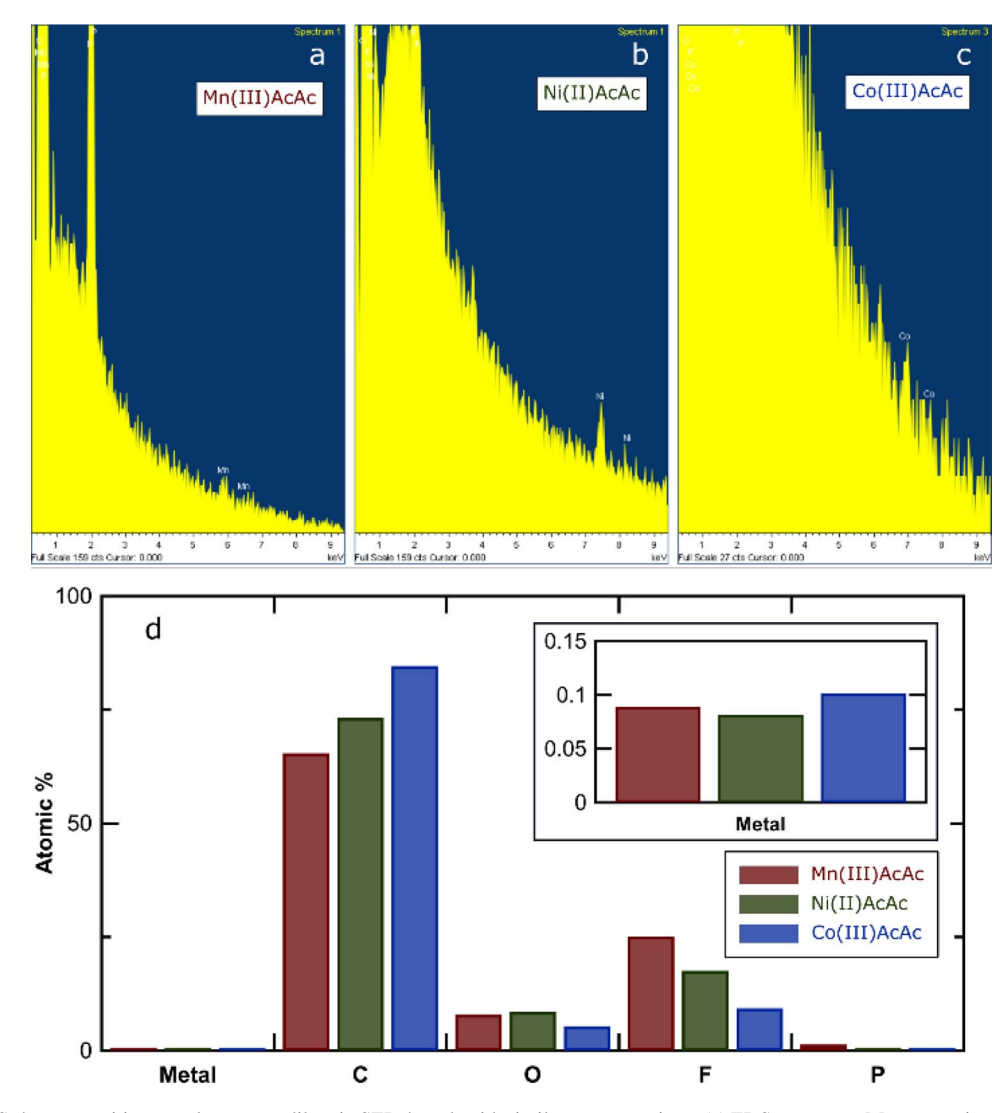
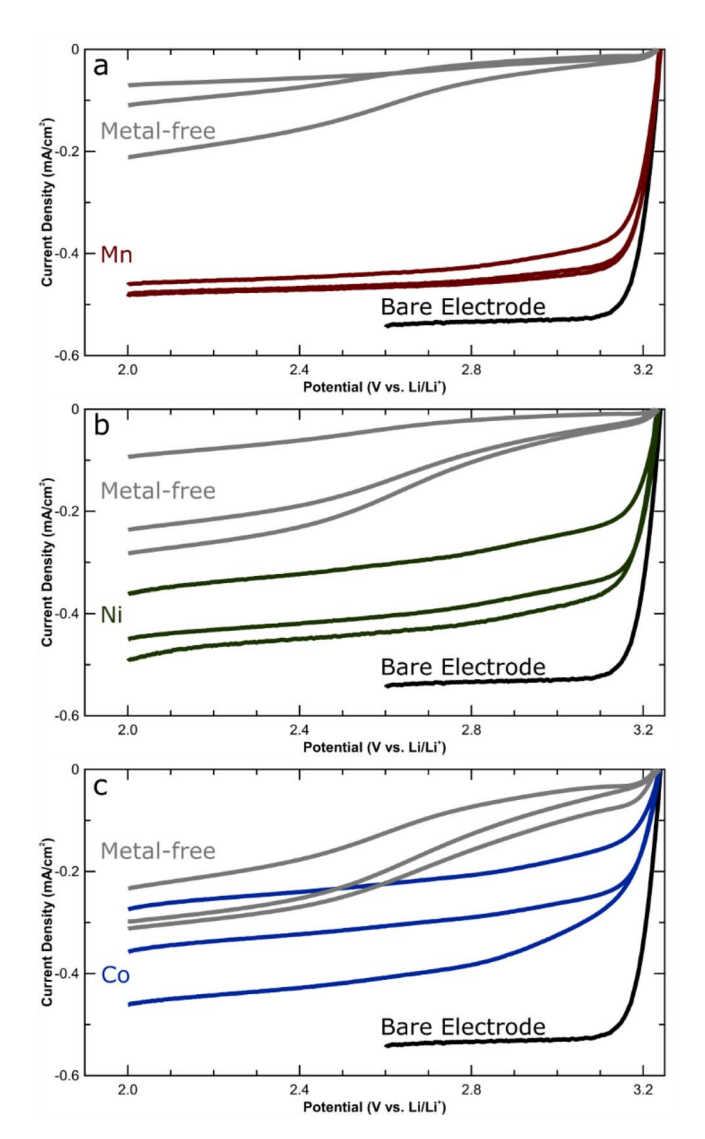


Figure 2. SEM/EDS shows transition metals are very dilute in SEI, though with similar concentrations. (a) EDS spectra on Mn-contaminated SEI; (b) EDS spectra on Ni-contaminated SEI; (c) EDS spectra on Co-contaminated SEI; (d) Summary of atomic % found by EDS for each metal with inset showing atomic % of each metal.



**Figure 3.** Transition metal contamination impedes SEI passivation. (a) Ferrocenium reduction voltammograms on Mn-contaminated SEI (red), metal-free SEI (gray), and bare electrode (black); (b) Ferrocenium reduction voltammograms on Ni-contaminated SEI (green), metal-free SEI (gray), and bare electrode (black); (c) Ferrocenium reduction voltammograms on Co-contaminated SEI (blue), metal-free SEI (gray), and bare electrode (black).

trolyte. Although signal from the underlying substrate and the inherent limitations of EDX make quantitative composition of the films difficult, Figure 2d confirms the presence of the three metals. Additionally, Figure 2d indicates that the metals are each extremely dilute and of similar concentrations across the films, in accordance with results using more sensitive techniques such as ICP-OES.<sup>37</sup>

Effects of transition metals on SEI passivity.—Ferrocenium reduction profiles for each of the transition metals under study are presented in Figure 3. The black lines show ferrocenium reduction on a bare electrode without a passivation layer, demonstrating reversible reduction kinetics and transport limits described by the Levich equation. <sup>49</sup> Grey lines show ferrocenium reduction through a metalfree SEI formed on the same glassy carbon discs, while colored lines are for a metal-contaminated SEI (3a, Mn; 3b, Ni; and 3c, Co). Three trials are presented for each metal, demonstrating reasonable reproducibility.

Figure 3 indicates that these metals have similar effects on SEI passivity, though to varying degrees. As expected, in all cases a metal-contaminated SEI less effectively blocks charge transfer from the

working electrode to the ferrocenium ions when compared to a metalfree SEI. However, a SEI formed in the presence of Mn allows far more ferrocenium reduction than a SEI formed with Ni or Co present, consistent with coulombic efficiency and lifetime trends in full-cell Li-ion batteries.<sup>4,37</sup>

Various models can describe SEI passivation as well as the mechanisms by which transition metals disrupt this passivation. Figure 4 contains graphical and equivalent circuit representations of the metal-contaminated SEI and metal-free SEI in the RDE experimental setup. The green layer indicates the compact, inner SEI while the purple arrows represent electrolyte or mediator transport through the porous, outer SEI layer. White arrows show electron transport from the working electrode to a reaction site. Metal-free pinholes are thin and black while metallic pinholes are wide. Red ovals show catalytic sites for metal redox cycling.

Figure 4a represents a metal-free SEI and an equivalent circuit of this SEI is shown in Figure 4b as a series of resistors including a Levich resistance, associated with mass transfer from the bulk electrolyte to the diffusion layer as a function of rotation speed; a 2D-diffusion resistance, signifying mass transport through the film to the pinhole; a kinetic resistance for ferrocenium or electrolyte reduction at the pinhole; and an ohmic resistance for electron transport from the electrode to the pinhole. The total current through this circuit is denoted as  $i_{metal-free}$ , and the current through the SEI portion is  $i_{PH}$ , pinhole current.

As previously discussed,  $^{32}$  one way to conceptualize the effects of metal contamination is that active sites within the SEI become more plentiful and more active with the incorporation of transition metals, such as in Figure 4c. In other words, metals within the film act as additional sites with greater activity, but do not follow a separate mechanism for ferrocenium reduction, as represented in Figure 4d. Here the 2D-diffusion, kinetic, and ohmic resistances are modified to include both non-metallic and metallic pinholes. The effect of metal contamination is to lower these resistances to ferrocenium reduction, analogous to increased SEI degradation in a true battery. The total current through this equivalent circuit is denoted as  $i_{tot}$ , total current, and the portion through the SEI is  $i_{PH} + i_{metal}$ . Figure 4e and Figure 4f illustrate a metal-contaminated SEI under a mechanism proposed by Joshi and others  $^{4,22,23,25,42}$  and will be further discussed in Part II.

In order to better understand the effects of transition metal contamination on charge transfer through the SEI, we employed a simple model<sup>38</sup> that treats ferrocenium reduction with Butler-Volmer kinetics and a through-film transport resistance, such as in Figure 4b and Figure 4d. Figure 5 shows our model (red) overlay over our experimental data (black) for one trial with a Mn-contaminated SEI. Comparing the effective rate constants,  $k_{eff}$ , and the through-film limiting currents,  $i_{lim,f}$ , used to fit our model to experimental data reveals the extents to which each metal disrupts the passivation of the SEI

As shown in Figure 6, ferrocenium reduction through an SEI contaminated by Mn occurs with faster kinetics (a) and through-film transport (b) than both Ni and Co. There is some variation between the fitting parameters describing ferrocenium reduction through a metalfree SEI on the three different glassy-carbon electrodes, which is likely a consequence of the unique surfaces on each electrode, even after polishing. 50,51 The extent to which each metal interferes with passivation against ferrocenium reduction is determined by the ratio of metal-contaminated and metal-free average kinetic and transport parameter in Figure 7. The most important difference between the three metals is the Butler-Volmer kinetics of ferrocenium reduction, with the effect of Mn-contamination (left, red) almost an order of magnitude greater than that for Co-contamination (left, blue). Through-film transport is also fastest when the SEI contains Mn, though this result is not as dramatic. These results clearly show that Mn interferes with SEI passivation to a much greater extent than the other common highvoltage Li-ion battery transition metals (Ni and Co), which is consistent with conventional knowledge and substantiates why research is vastly more focused on inhibiting Mn contamination. However, the

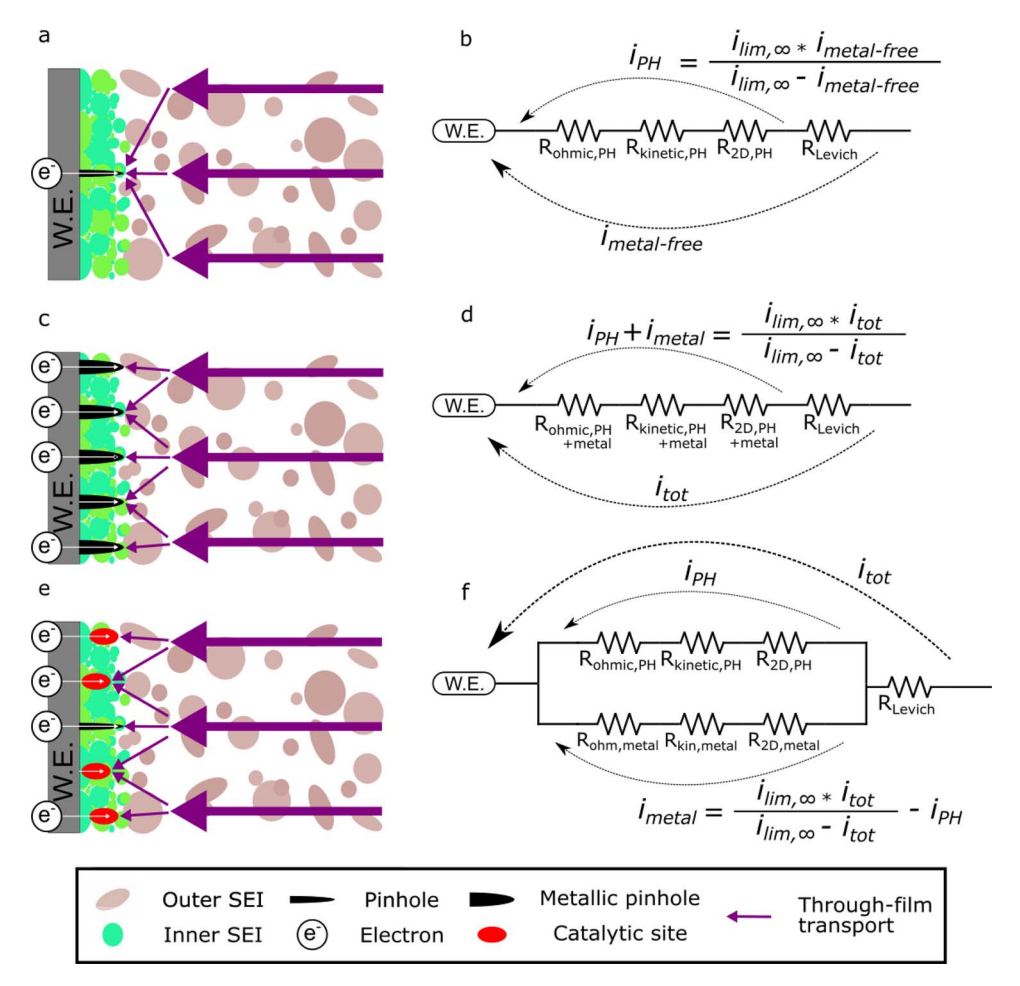
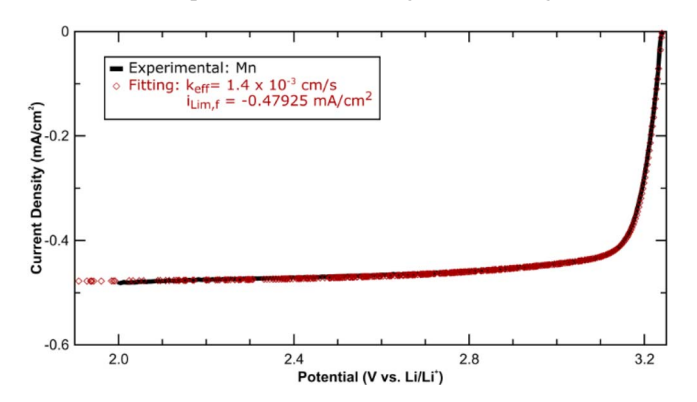


Figure 4. Possible mechanisms of SEI interference by metals and equivalent circuits of SEI transport and kinetics under these mechanisms. (a) Charge transfer through a metal-free SEI with a pinhole; (b) Equivalent circuit of metal-free SEI with a pinhole; (c) Charge transfer through a metal-contaminated SEI with metallic pinholes; (d) Equivalent circuit of metal-contaminated SEI with metallic pinholes; (e) Charge transfer through a metal-contaminated SEI with a pinhole and metallic catalytic sites for metal-mediated SEI degradation; (f) Equivalent circuit of metal-contaminated SEI with a pinhole and metallic catalytic sites.

results here further indicate that kinetics are much more sensitive than transport, which indicates stronger effects of Mn on electronic than morphological properties.

Differences between transition metals: Butler-Volmer kinetics at isolated pinholes.—The differences between transition metals may be interpreted in the context of a physics-based model proposed in our previous work.<sup>32</sup> In this model, charge-transfer through the SEI occurs at isolated pinholes, such as in Figure 4a and Figure 4c. Two-



**Figure 5.** Model incorporating Butler-Volmer kinetics and a through-film limiting current adequately describes ferrocenium reduction through a metal-contaminated SEI.

dimensional diffusion limits to these pinholes result in the following expression for the through-film limiting current:

$$i_{lim,f} = \frac{nFAD_{O,f} \chi_O C_{O,\infty}}{\phi + \frac{2R_0}{\sqrt{1-\theta}}}$$
[1]

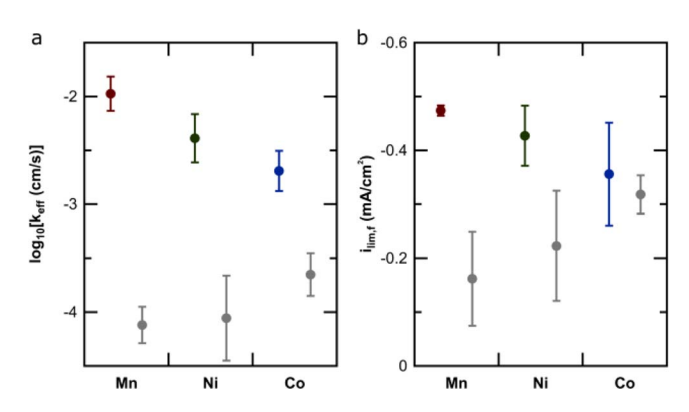


**Figure 6.** Fitting parameters for the metal-contaminated and metal-free SEI formed on glassy-carbon electrodes. Circles represent mean of three trials, error bars represent one standard deviation. Grey series represent metal-free trials on the same glassy-carbon electrodes (a) Butler-Volmer effective kinetic rate constants,  $k_{eff}$ ; (b) Through-film limiting currents,  $i_{lim,f}$ .

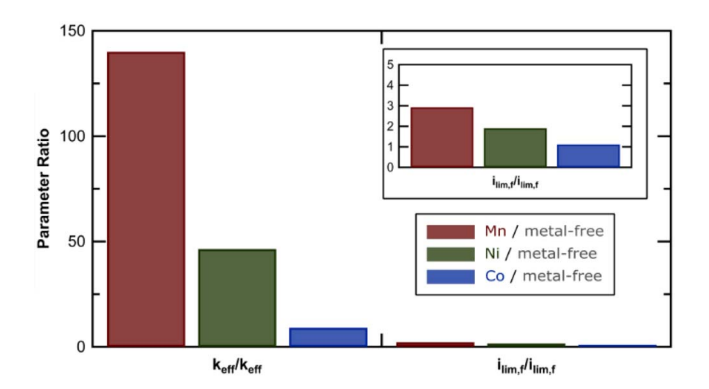


**Figure 7.** Extent of SEI passivation disruption by each metal. Values calculated by dividing the metal-contaminated parameter by the metal-free SEI parameter.

Nomenclature is listed in Table A-I.  $I-\theta$  represents the area fraction of pinholes within the blocking film, and  $2R_0$  represents the average center-to-center distance of the pinholes. Assuming that the diffusion distance to the pinholes,  $\frac{2R_0}{\sqrt{I-\theta}}$ , dominates over the diffusion distance through the outer SEI layer,  $\phi$ ,

$$i_{lim,f} \propto \frac{\sqrt{1-\theta}}{2R_0}$$
 [2]

Thus, the increase in through-film limiting current through a Mn-contaminated SEI compared to a Ni- or Co-contaminated SEI can be attributed to either an increase in number or size of pinholes, or a decrease in distance between pinholes, assuming that the surface area, A, through-film diffusion coefficient,  $D_{O,f}$ , partition coefficient,  $\chi_O$ , and bulk ferrocenium concentration, $C_{O,\infty}$ , remain the same across films. The radius of the pinholes is geometrically tied to the center-to-center distance and the area fraction of pinholes by the following relation:<sup>52</sup>

$$R_a = R_0 \sqrt{1 - \theta} \tag{3}$$

The effective rate constant is related to the area fraction of active sites by:

$$k_{eff} = k_0 (1 - \theta) (\chi_O)^{\alpha_c} (\chi_R)^{\alpha_a}$$
 [4]

The results in Figure 6 and Figure 7 clearly demonstrate that transition metals affect electronic properties of the SEI more drastically than morphological properties, and that Mn is most disruptive to the electronic properties compared to Ni or Co. Figure 8 demonstrates this conclusion graphically. If it is assumed that there are no electronic differences between a Mn-contaminated and Co-contaminated SEI, i.e.  $k_{0,Mn} = k_{0,Co}$ , then the area fraction of Mn within the film would need to be at least fifteen times greater than that of Co (Figure 8a, area fraction shown to scale). Higher Mn than Co composition contradicts our EDX findings in Figure 2 as well as observations by other groups<sup>37</sup> with the more sensitive ICP-OES technique. A fifteen-fold difference in area fraction of Mn to Co therefore seems very unlikely, and we conclude there must exist an inherent electronic difference in a SEI contaminated by these metals. In the other limiting case, the area fractions of metals within the film are equal, i.e.  $1 - \theta_{Mn} = 1 - \theta_{Co}$ . As represented in Figure 8b, the Mn pinholes must be smaller than the Co pinholes to satisfy the difference in through-film limiting current,  $i_{lim,f}$ , according to Eqs. 2 and 3 such that:

$$\frac{R_{a,Mn}}{R_{a,Co}} \propto \frac{i_{lim,f,Co}}{i_{lim,f,Mn}}$$
 [5]

Constraining  $1-\theta$  results in fifteen-fold faster electron transfer rate with Mn than with Co, i.e.  $k_{0,Mn}=15k_{0,Co}$ . In an intermediate case, not shown in Figure 8, equal pinhole spacing for Mn and Co, i.e.  $R_{0,Mn}=R_{0,Co}$ , implies that both the electron transfer rate and area fraction of Mn are greater than for Co. Ultimately, analysis of  $i_{lim}$  and  $i_0$  concludes that Mn alters the electronic properties of the SEI to a greater extent than Ni and Co. Figure 2 and previous literature indicate that the concentrations of metals within the film are on the same order of magnitude, which lends support to the assumption in Figure 8b Case II. The increased rate of electron transfer at Mn pinholes vs Co pinholes remains unexplained.

Effects of metal dopants on bandgaps of Li<sub>2</sub>CO<sub>3</sub> and LiF crystals.—The combined results of Figure 6 and Figure 7 show that Mn, Ni, and Co affect the through-film kinetics of the SEI much more than through-film transport, and the analysis of Figure 8 shows that coverage effects are unlikely to explain these differences. Thus, transition metals much affect the SEI's electronic properties much more than they affect its morphology. Based on our previous conclusions that inorganic SEI components such as LiF and Li<sub>2</sub>CO<sub>3</sub> are responsible for the SEI's electronic insulating properties, we hypothesized that transition metals function as dopants in the SEI's inorganic

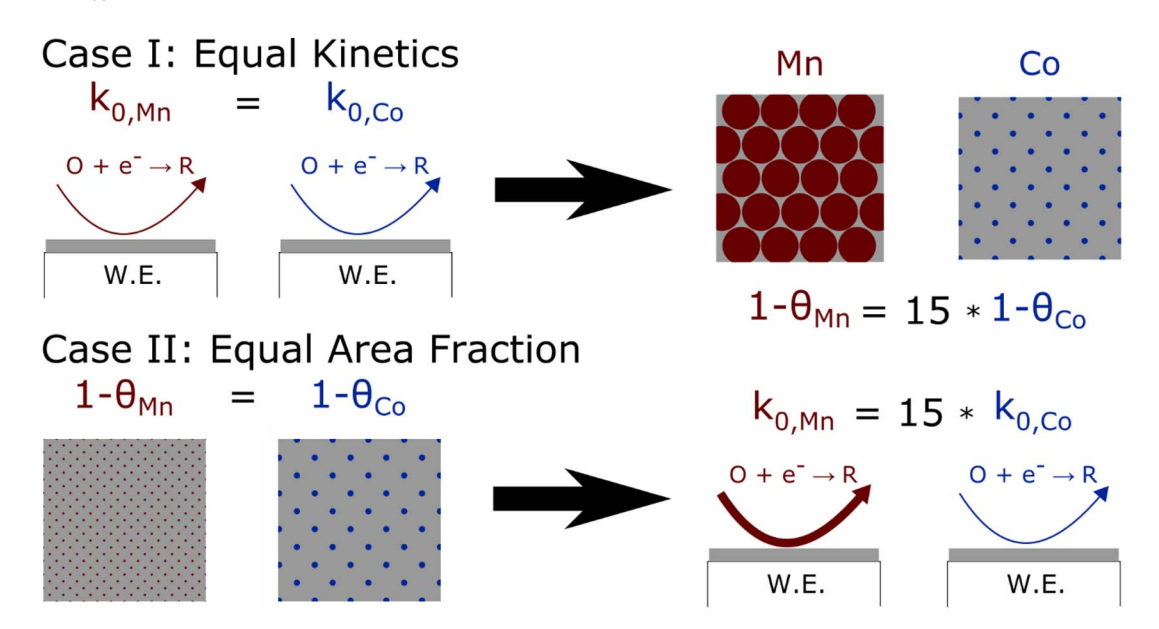


Figure 8. Exploring possible physical interpretations of measured differences between metal-contaminated films with two limiting cases: where the electron transfer rate,  $k_0$ , for the two metals are equal, and where the area fraction,  $1 - \theta$ , are equal. Physical parameters  $1 - \theta$ ,  $R_0$ , and  $R_a$  are shown to scale.

Table I. Calculated bandgap energies for metal-doped LiF and  $\text{Li}_2\text{CO}_3$ .

Metal	Band gap in $\text{Li}_{0.9815}\text{M}_{0.0093}\text{F}$ (eV)	Band gap in $(Li_{1.5}M_{0.25}CO_3)_4$ (eV)
None	8.7	4.95
$Mn^{2+}$	7.52	4.05
Ni <sup>2+</sup>	1.16	2.13
$Co^{2+}$	5.52	2.49
$Mn^0$		2.3
$Ni^0$		1.4
$Co^0$		~0.5

components. Introducing metal dopants to these wide-bandgap semi-conductors could reduce the effective bandgap and therefore the tunneling barrier to reaction. Different metals would therefore have very different effects on the SEI passivity, depending on specific electronic interactions between Mn, Ni, and Co and LiF or  $\text{Li}_2\text{CO}_3$ .

To test this hypothesis, the electronic densities of states were calculated for Li $_{0.9815}M_{0.0093}F$  and (Li $_{1.5}M_{0.25}CO_3$ ) $_4$  with M = Mn $^{2+}$ , Ni $^{2+}$ , and Co $^{2+}$ . A sample calculation for LiF is shown in Figure 9, and the results for both compounds are summarized in Table I.

The left half of Fig. 9 depicts the electronic orbital densities of states (DOS) for LiF crystals with two nearest neighbor Li ions substituted by a single M<sup>2+</sup>, where M can be sextet Mn, triplet Ni, or doublet Co. The Fermi level in each case is sensitive to the occupancy of the transition metal d-orbitals. All three metal ions exhibit gaps in the state represented by down-spin d-orbitals, the energy levels of which vary significantly. For  $Co^{2+}$  and  $Ni^{2+}$ , the gaps between the occupied valence states and the unoccupied d-orbital states are drastically reduced from the case if the transition metal would not be there (Table I). In contrast, the unoccupied Mn<sup>2+</sup> d-orbital is located near the conduction band edge. Mn therefore minimally modifies the gap between the occupied and unoccupied states, and its mid-gap d-orbitals should provide the least favorite conduit for electron transport through the LiF crystal. For completeness, on the right half of Fig. 9, an electron is added and a Li<sup>+</sup> fills the lithium vacancy not occupied by the transition metal ion to retain charge neutrality. In other words, these DOS come from electrochemical reduction of the transition metal ions and the subsequent diffusion of a Li<sup>+</sup> next to the transition metal ions. The now-occupied Mn mid-gap state remains highest in orbital energy, showing that  $\dot{M}^{2+}$  and  $\dot{M}^{+}$  dopants exhibit the same trends between metals.

Similar DFT calculations were performed to find the density of states (DOS) for doped Li<sub>2</sub>CO<sub>3</sub> crystals and were consistent with those performed on LiF. The bandgaps for all doped and undoped crystal structures are summarized in Table I. For pure Li<sub>2</sub>CO<sub>3</sub>, the spin-up

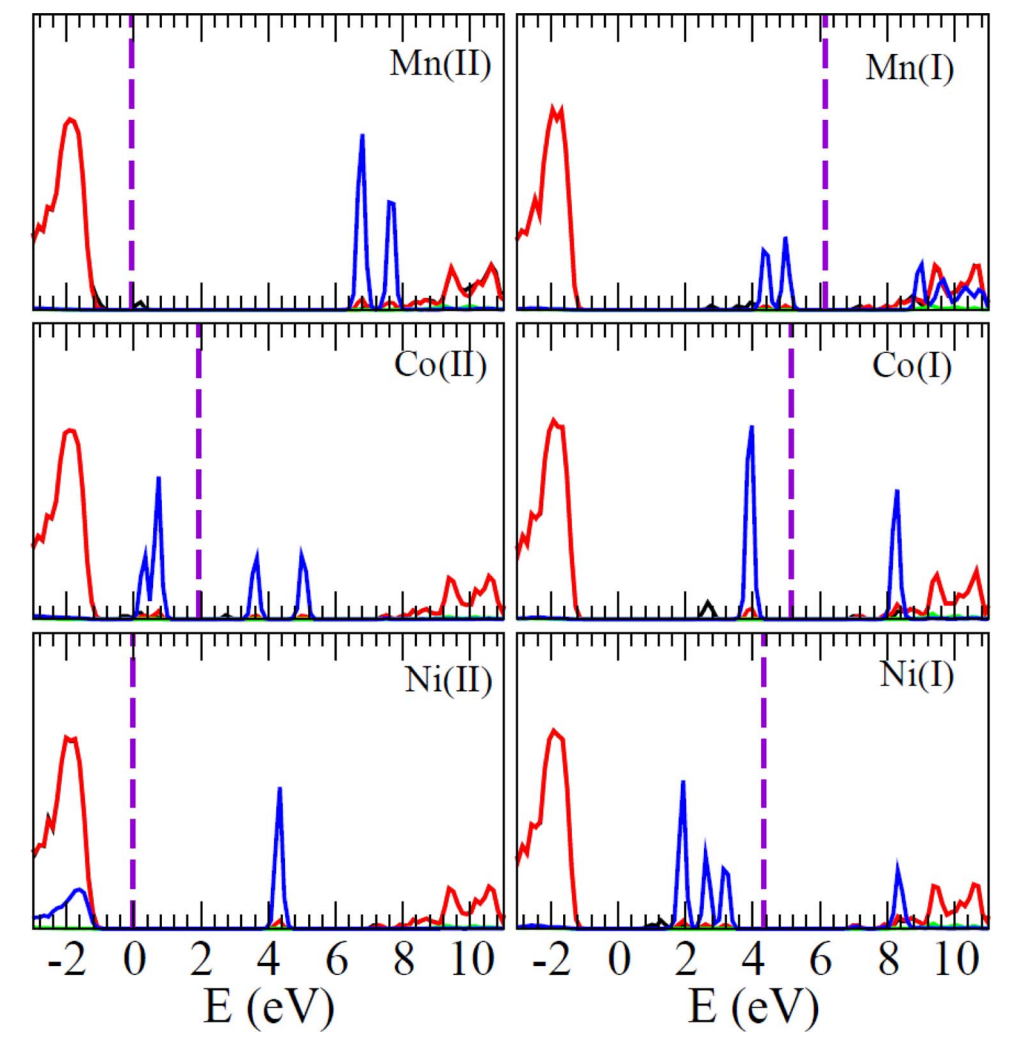


Figure 9. Calculated electronic densities of state (DOS) for Mn-, Ni-, and Co-doped LiF. Black/red lines represent the total up/down spin DOS, while green/blue lines are up/down spin d-orbital contributions from the transition metal ions. The total- and d-orbital-sets are not normalized to the same scale. Violet dashed lines indicate the Fermi levels.

and spin-down DOS were identical, and the calculated bandgap was 4.95 eV. Similar to the trend observed with LiF, when doped with Mn<sup>2+</sup>, new peaks were observed in the spin down DOS near the conduction band edge, resulting in a decreased bandgap to 4.05 eV. For Ni<sup>2+</sup> and Co<sup>2+</sup> doping, the new peaks were located in the original bandgap of pure Li<sub>2</sub>CO<sub>3</sub>, dramatically diminishing the bandgap to 2.13 eV and 2.49 eV, respectively. Furthermore, when doped with Mn<sup>0</sup>, Ni<sup>0</sup>, and Co<sup>0</sup>, the bandgaps were further diminished compared to the corresponding +2 ion doping. The reduced Co<sup>0</sup> and Ni<sup>0</sup> caused much smaller bandgaps of Li<sub>2</sub>CO<sub>3</sub>. Additional calculations (not shown) found the same trends between metals at different redox states.

In summary, the calculations show that Mn has by far the weakest effect on the bandgap of both LiF and Li<sub>2</sub>CO<sub>3</sub>, while Co introduces the most states in the bandgap. Because the smallest bandgap should have the lowest electron tunneling barrier, the calculations therefore predict that Co should yield the least passivating SEI while Mn has minimal effect. However, the experiments presented here show the exact opposite trend. There are two major explanations for this discrepancy. First, the SEI is not a single crystal of LiF or Li<sub>2</sub>CO<sub>3</sub>. Experimental and theoretical studies have shown that electron transfer occurs preferentially at grain boundaries and other defects. 53,54 If Mn introduces intrinsically different types of defects than Ni or Co, simple atomic models will be unable to accurately describe the electron transport properties at those sites. We are currently exploring these possibilities through modeling and experiment. Alternatively, the model of simple electron tunneling across the SEI may itself be incomplete if the transition metals participate in a catalytic redox cycle, as proposed by Joshi and others. 4,22,23,25,42 If this is the case, the standard Butler-Volmer expression cannot adequately describe the overall reaction rate. We have investigated this possibility by deriving a microkinetic model of the redox cycling mechanism and comparing it to experiment. The model development and corresponding results are presented in Part II.

## Conclusions

RDE experiments and physics-based models of experimental data clearly demonstrate that the reduction kinetics of a reversible ferrocenium mediator are much more rapid through the metal-contaminated than the metal-free SEI. Controlled introduction of Mn, Ni, and Co cations shows that through-film kinetics are much faster through a Mn-contaminated SEI than through an SEI contaminated by Ni or Co. Through film transport follows the same trend, though to a much lesser degree. These results both confirm previous work documenting the particularly disruptive nature of Mn in the SEI compared to these other metals and further this understanding by identifying that the electronic rather than the morphological properties of the SEI are most impacted by metal contamination. Although the unique effect of Mn on SEI passivity is unambiguous, DFT simulations do not support the hypothesis that Mn decreases the bandgap of common SEI compounds more than Ni and Co. This inconsistency lends further support to an alternative mechanism of charge transfer through SEI based on metal redox cycling, which is explored in Part II of this work.

#### Acknowledgments

This work was supported by NSF-1751553. YXL and YQ acknowledge the National Science Foundation through grant number DMR-1832808. KL is was supported by Nanostructures for Electrical Energy Storage (NEES), an Energy Frontier Research Center funded by the U.S. Department of Energy, Office of Science, Office of Basic Energy Sciences under Award Number DESC0001160. Sandia National Laboratories is a multi-mission laboratory managed and operated by National Technology and Engineering Solutions of Sandia, LLC, a wholly owned subsidiary of Honeywell International, Inc., for the U.S. Department of Energy's National Nuclear Security Administration under contract DE-NA0003525. This paper describes objective technical results and analysis. Any subjective views or opinions that might be

expressed in the paper do not necessarily represent the views of the U.S. Department of Energy or the United States Government.

#### **Appendix**

#### Table A-I. List of Symbols and Meanings.

$\alpha_a$	Anodic charge transfer coefficient
$\alpha_c$	Cathodic charge transfer coefficient
θ	Fractional coverage of electrode by blocking film
ф	Outer SEI layer thickness
χο	Partition coefficient of oxidized species from bulk to
	film
XR	Partition coefficient of reduced species from bulk to
	film
A	Electrode surface area
$C_{o,\infty}$	Bulk concentration of ferroceniumin solution
$D_{o,f}$	Effective diffusivity of oxidized species in film
F	Faraday's constant
$i_{lim, f}$	Through-film limiting current
$i_{lim,\infty}$	Limiting current on a pristine electrode
$i_{metal}$	Current attributed to metal catalytic sites
$i_{metal-free}$	Total current through metal-free SEI
$i_{pH}$	Current attributed to pinholes
$\hat{i_{tot}}$	Total current through metal-contaminated SEI
$k_0$	Electron transfer rate
$k_{eff}$	Effective heterogeneous rate constant
n	Number of electrons transferred in redox reaction
$2R_0$	Average pinhole center-to-center distance
$R_a$	Pinhole radius
$R_{2D,PH}$	Mass transfer resistance of 2D-diffusion to pinholes
$R_{2D,PH+metal}$	Mass transfer resistance of 2D-diffusion to metallic
	and nonmetallic pinholes
$R_{2D,metal}$	Mass transfer resistance of 2D-diffusion to metal
	catalytic sites
$R_{Levich}$	Mass transfer resistance from the bulk electrolyte to
	the diffusion layer
$R_{kinetic,PH}$	Kinetic resistance at pinholes
$R_{kinetic,PH+metal}$	Kinetic resistance at metallic and nonmetallic pinholes
$R_{kin,metal}$	Kinetic resistance at metal catalytic sites
$R_{ohmic,PH}$	Ohmic resistance at pinholes
$R_{ohmic,PH+metal}$	Ohmic resistance at metallic and nonmetallic
,	pinholes
$R_{ohm,metal}$	Ohmic resistance at metal catalytic sites

### **ORCID**

Oliver C. Harris https://orcid.org/0000-0002-5484-5688 Maureen H. Tang https://orcid.org/0000-0003-0037-4814

#### References

- 1. D. H. Jang, Y. J. Shin, and S. M. Oh, J. Electrochem. Soc., 143, 2204 (1996).
- H. Zheng, Q. Sun, G. Liu, X. Song, and V. S. Battaglia, J. Power Sources, 207, 134 (2012).
- 3. J. A. Gilbert et al., J. Electrochem. Soc., 164, A6054 (2017).
- J. A. Gilbert, I. A. Shkrob, and D. P. Abraham, J. Electrochem. Soc., 164, A389 (2017).
- 5. D. R. Gallus et al., *Electrochim. Acta*, 134, 393 (2014).
- 6. I. Buchberger et al., *J. Electrochem. Soc.*, **162**, A2737 (2015).
- D. P. Abraham, T. Spila, M. M. Furczon, and E. Sammann, *Electrochem. Solid-State Lett.*, 11, A226 (2008).
- 8. X. Liao et al., J. Power Sources, 286, 551 (2015).
- 9. Y. Xia, J. Electrochem. Soc., 144, 2593 (1997).
- 10. L. Yang, M. Takahashi, and B. Wang, Electrochim. Acta, 51, 3228 (2006).
- 11. W. Choi and A. Manthiram, J. Electrochem. Soc., 153, A1760 (2006).
- 12. S. R. Gowda et al., Phys. Chem. Chem. Phys., 16, 6898 (2014).
- N. P. W. Pieczonka et al., *J. Phys. Chem. C*, **117**, 15947 (2013).
  S. Komaba, N. Kumagai, and Y. Kataoka, *Electrochim. Acta*, **47**, 1229 (2002).
- 15. C. Delacourt et al., *J. Electrochem. Soc.*, **160**, A1099 (2013).
- 16. C. Zhan et al., *Nat. Commun.*, **4**, 1 (2013).
- 17. Y. Li et al., J. Electrochem. Soc., 160, A3006 (2013).

- 18. D. Lu, M. Xu, L. Zhou, A. Garsuch, and B. L. Lucht, J. Electrochem. Soc., 160, A3138 (2013).
- 19. M. Ochida et al., J. Electrochem. Soc., 159, A961 (2012).
- 20. T. Tsujikawa, K. Yabuta, T. Matsushita, M. Arakawa, and K. Hayashi, J. Electrochem. Soc., 158, A322 (2011).
- 21. X. Xiao et al., Phys. Chem. Chem. Phys., 16, 10398 (2014).
- 22. I. a. Shkrob et al., J. Phys. Chem. C, 118, 24335 (2014).
- 23. D. R. Vissers et al., ACS Appl. Mater. Interfaces, 8, 14244 (2016).
- 24. S. Solchenbach, G. Hong, A. T. S. Freiberg, R. Jung, and H. A. Gasteiger, J. Electrochem. Soc., 165, A3304 (2018).
- 25. T. Joshi, K. Eom, G. Yushin, and T. F. Fuller, J. Electrochem. Soc., 161, A1915 (2014).
- 26. A. Jarry et al., J. Am. Chem. Soc., 137, 3533 (2015).
- 27. J. Wandt et al., J. Mater. Chem. A, 4, 18300 (2016).
- 28. H. Tsunekawa et al., J. Electrochem. Soc., 149, A1326 (2002).
- 29. E. Peled, J. Electrochem. Soc., 126, 2047 (1979).
- 30. K. Xu, Chem. Rev., 104, 4303 (2004).
- K. Xu, Chem. Rev., 114, 11503 (2014).
  O. C. Harris and M. H. Tang, J. Phys. Chem. C, 122, 20632 (2018).
- 33. J. M. Tarascon, J. Electrochem. Soc., 138, 2859 (1991).
- 34. M. Börner et al., J. Electrochem. Soc., 163, A831 (2016).
- 35. S. Komaba et al., J. Electrochem. Soc., 152, A937 (2005).
- 36. A. Banerjee et al., J. Am. Chem. Soc., jacs.6b10781 (2017).
- 37. R. Jung et al., J. Electrochem. Soc., 166, A378 (2019).
- 38. M. Tang and J. Newman, J. Electrochem. Soc., 158, A530 (2011).

- 39. M. Tang, S. Lu, J. Newman, E. T. Division, and L. Berkeley, J. Electrochem. Soc., 159, A1775 (2012).
- 40. M. Tang, J. Newman, E. Technologies, and L. Berkeley, J. Electrochem. Soc., 159, A281 (2012).
- 41. M. Tang and J. Newman, J. Electrochem. Soc., 159, A1922 (2012).
- 42. K. Leung, Chem. Mater., 29, 2550 (2017).
- 43. G. Kresse and J. Furthmüller, *Phys. Rev. B*, 54, 11169 (1996).
- 44. J. Paier, M. Marsman, and G. Kresse, J. Chem. Phys., 127, 024103 (2007).
- 45. G. Kresse and D. Joubert, *Phys. Rev. B*, **59**, 1758 (1999).
- 46. J. P. Perdew, K. Burke, and M. Ernzerhof, Phys. Rev. Lett., 77, 3865 (1996).
- 47. S. L. Dudarev, G. A. Botton, S. Y. Savrasov, C. J. Humphreys, and A. P. Sutton, *Phys.* Rev. B, 57, 1505 (1998).
- 48. M. Tang, K. Miyazaki, T. Abe, and J. Newman, J. Electrochem. Soc., 159, A634 (2012).
- 49. A. J. Bard and L. R. Faulkner, Electrochemical Methods Fundamentals and Applications, 2nd ed., Wiley, New York, (2001).
- 50. R. M. Wightman, M. R. Deakin, P. M. Kovach, W. G. Kuhr, and K. J. Stutts, Methods to Improve Electrochemical Reversibility at Carbon Electrodes. J. Electrochem. Soc., 131(7), 1578 (1984)
- 51. G. Zampardi, F. La Mantia, and W. Schuhmann, *RSC Adv.*, 5, 31166 (2015).
- 52. J.-M. Saveant, *J. Electroanal. Chem.*, **302**, 91 (1991).
- 53. Q. Zhang et al., Nano Lett., 16, 2011 (2016).
- 54. J. Ko and Y. S. Yoon, Ceram. Int., 45, 30 (2019).
- 55. O. C. Harris, K. Leung, and M. H. Tang, J. Electrochem. Soc., 167, 013503 (2020).